Lithium Electrodeposition Dynamics in Aprotic Electrolyte Observed *in Situ via* Transmission Electron Microscopy

Andrew J. Leenheer,* Katherine L. Jungjohann, Kevin R. Zavadil, John P. Sullivan, and C. Thomas Harris*

Center for Integrated Nanotechnologies, Sandia National Laboratories, Albuquerque, New Mexico 87185, United States

ABSTRACT Electrodeposited metallic lithium is an ideal negative battery electrode, but nonuniform microstructure evolution during cycling leads to degradation and safety issues. A better understanding of the Li plating and stripping processes is needed to enable practical Li-metal batteries. Here we use a custom microfabricated, sealed liquid cell for *in situ* scanning transmission electron microscopy (STEM) to image the first few cycles of lithium electrodeposition/dissolution in liquid aprotic electrolyte at submicron resolution. Cycling at current densities from 1 to 25 mA/cm^2 leads to variations in grain structure, with higher current densities giving a more needle-like, higher surface area deposit. The effect of the electron beam was explored, and it was found that, even with minimal beam exposure, beam-induced surface film formation could alter the Li microstructure. The electrochemical dissolution was seen to initiate from isolated points on grains rather than uniformly across the Li surface, due to the stabilizing solid electrolyte interphase surface film. We discuss the implications for *operando* STEM liquid-cell imaging and Li-battery applications.

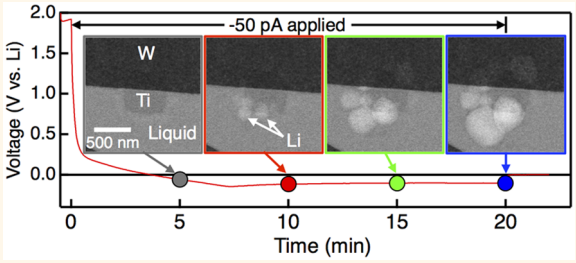

KEYWORDS: lithium electrodeposition · liquid-cell electron microscopy · electron beam radiolysis · lithium-ion battery · solid electrolyte interphase · *in situ* TEM

High energy density, long-lasting rechargeable batteries are highly desirable for applications in consumer electronics and electric vehicles, but the substantial volume and weight of electrochemically inactive components of the battery electrodes limit current technologies. Metallic lithium is, theoretically, an optimal negative electrode (anode during discharge) for Li-ion battery chemistry with the most negative standard reduction potential of −3.01 V and a high specific capacity of 3.86 Ah/g (2.06 Ah/cm^3).[1] However, upon repeated charge/discharge cycles, variations in the lithium plating and stripping morphology result in high-surface-area deposits.[1−4] Because most electrolytes decompose once in contact with metallic lithium, a stabilizing surface film, termed a "solid electrolyte interphase" (SEI),[1,5] is formed on fresh Li surfaces during each cycle. The formation and presence of the SEI consumes electrolyte, immobilizes Li, and further magnifies the deleterious effects of nonuniformities during electrodeposition/dissolution. In extreme (but technologically relevant) cases, long Li dendrites can electrically short batteries, resulting in self-heating and explosions. In this work, we image Li electrodeposition from a typical Li-ion battery electrolyte using bright-field scanning transmission electron microscopy (BF STEM) to better understand the microstructural evolution of Li electrodes and to identify mechanisms that may lead to cell failure.

Compared to the generally used *post mortem* analysis, in which electrodes are rinsed and exposed to oxidizing environments that can alter both the surface and morphology of the mechanically compliant Li, imaging the Li electrodes *in situ* provides a more accurate assessment of the deposition morphology. Arguably, the simplest *in situ* imaging technique is visible-light microscopy, in which Li electrodes have been observed to form dendrites that kink and grow from either the dendrite base or tip[6,7] and sometimes rotate during growth.[8] In this dendritic growth process, the current density plays a critical role in the Li morphology (see Crowther and West[9] and the references therein for more on optical observations).

* Address correspondence to ajleenh@sandia.gov, ctharri@sandia.gov.

Received for review February 6, 2015 and accepted March 18, 2015.

Published online March 18, 2015
10.1021/acsnano.5b00876

Unfortunately, the micron-sized scale of a typical Li deposit approaches the resolution limit of visible light, especially for nucleation events, providing an unclear picture of the dendrite initiation and growth processes. Another *in situ* microscopy technique utilizes hard X-rays at a synchrotron beamline that can penetrate through relatively thick batteries, and X-ray tomography has shown the presence of subsurface defects below Li dendrites.[10] Electron microscopy provides very high resolution, and *in situ* imaging of electrochemical processes is possible with specialized electrochemical cells compatible with the high-vacuum environment. Scanning electron microscopy (SEM) has been used to show dendrite growth and electrical shorting in polymer[11,12] and ionic-liquid-based electrolytes,[13] but materials fully immersed in liquid electrolyte were not visible in these SEM studies due to the surface-sensitive nature of this microscopy technique. *In situ* TEM has provided a wealth of insight for materials changes during lithiation using "open" cells with solid or low-vapor-pressure ionic liquid electrolytes,[14,15] and observing materials immersed in the more relevant volatile liquid electrolytes is now possible in the TEM with the use of hermetically sealed liquid cells composed of electron-transparent membranes encapsulating a thin liquid layer. The use of TEM liquid cells is seeing applications in electrochemically induced processes such as Sn−Li film alloying,[16] Si nanowire lithiation,[17] and $LiFePO_4$ delithiation[18] as well as purely beam-induced processes such as nanoparticle growth,[19−26] lithiation,[27] and electrolyte decomposition.[28] Cu, Pb, and Ni electrodeposition have been successfully imaged and analyzed *in situ* using TEM liquid cells with aqueous electrolytes.[29−31] Li electrodeposition from aprotic solvent-based electrolytes involves experimentally more difficult material compatibility and purity considerations for the TEM liquid cell, and only a few low-contrast, ambiguous examples have been reported to date.[32,33]

In this work, we used a custom-designed TEM liquid cell[34] with relatively small (0.26 μm^2) working electrodes such that the entire active electrode could be observed with submicron resolution. The small electrode size ensured that all electrochemical charge passed could be quantitatively correlated with any visible changes, and carefully insulated leads enable pA-level current control. Each cell contained 10 total electrodes, allowing the ability to perform multiple experiments under identical chemical conditions by switching working electrodes. To simulate conditions in common Li-ion batteries with aprotic solvent-based electrolytes, the TEM liquid cell was filled with equal parts by volume of ethylene carbonate and dimethyl carbonate containing 1 M lithium hexafluorophosphate salt (1:1 EC:DMC/1 M $LiPF_6$). Li was electrodeposited onto inert Ti thin-film electrodes at varying current densities, and the formation of nonuniform, high-surface area Li deposits was clearly observed with

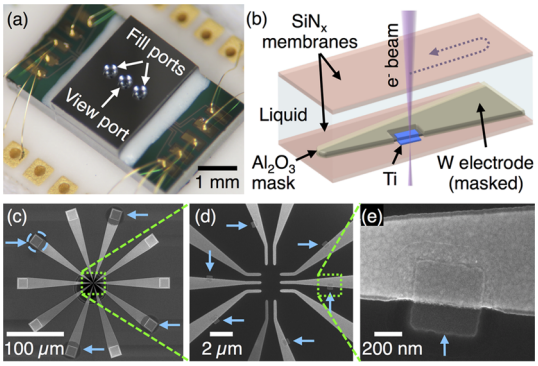

Figure 1. TEM liquid-cell design. (a) Sealed liquid cell wire-bonded to a ceramic carrier ready for electrolyte filling; (b) schematic of the geometry imaged in STEM mode; (c−e) scanning electron micrographs at increasing magnifications of the electrodes at the center of the bottom chip, where the patterned Ti electrode areas are noted with blue arrows.

the current density affecting the morphology. As the 300 keV electron beam can clearly induce electrolyte breakdown,[28,35] care was taken to minimize and characterize the effects of beam exposure. Through these efforts, we discovered that the electron beam both accelerated surface film formation and affected the deposition potentials and morphology, thus limiting the use of *operando* imaging during plating. The stripping dynamics also exhibited an interesting behavior, in which dissolution was initiated from discrete points on a Li grain. Our observations support SEI-mediated dendrite growth models and address the difficult-to-assess beam effects for liquid-cell TEM.

RESULTS AND DISCUSSION

The TEM liquid electrochemical cell used in this study[34] is shown in Figure 1 and comprises a bottom chip containing 10 electrodes that converge at the center of an electron-transparent SiN_x membrane window. The top chip, with a central SiN_x window and two fluid fill ports, was epoxy-sealed to the bottom chip to form the completed cell. Highly doped polycrystalline silicon electrical leads that connect the bond pads to the central metallic tungsten electrodes were insulated by thick SiO_2/SiN_x layers. The tungsten electrodes, residing at the center of the bottom chip, were further masked by a conformal Al_2O_3 layer to prevent contact with the electrolyte. Small, 0.26 μm^2 areas were lithographically defined near six of the electrode tips, and in these regions, the Al_2O_3 was etched away and a 35 nm thick Ti working electrode deposited as an inert substrate for the Li electrodeposition. Additionally, four electrodes were patterned with large, circular 750 μm^2 Ti patches out of the window region to serve as counter and quasireference electrodes. The cells used in this study displayed significant bowing of the SiN_x membranes, and the liquid layer was likely over a micron thick based on electron energy loss spectroscopy (EELS) measurements of the thickness, in which no

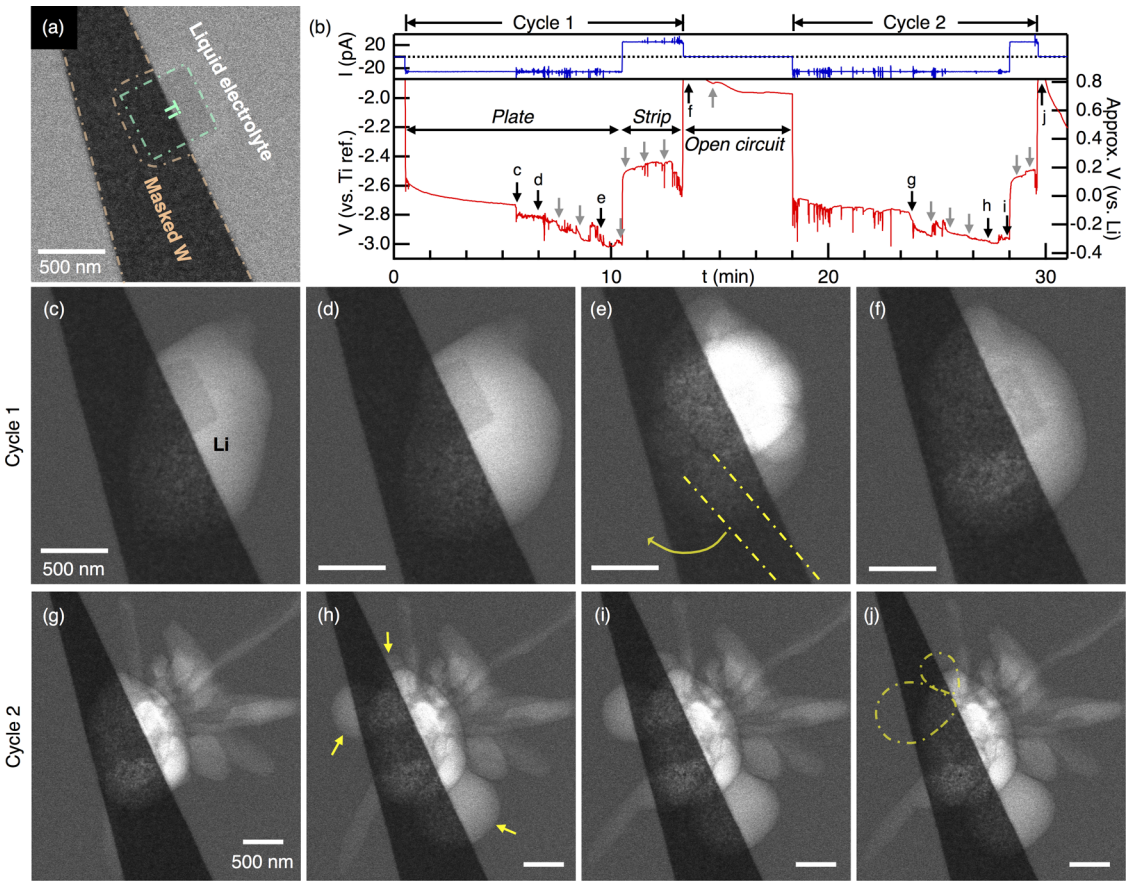

Figure 2. Time series of Li electrodeposition and stripping at $|J|$ = 10 mA/cm^2 shown in BF STEM images. (a) Electrode before applied current showing the Al_2O_3-masked tungsten electrode and an exposed 0.26 μm^2 Ti working electrode. (b) Applied current and resulting voltage measured *vs* a Ti quasireference electrode and the inferred voltage *vs* Li; a STEM image was taken at each arrow. First cycle plating (c−e) where a faint Li needle appeared in panel (e) outlined with yellow dotted lines and later rotated clockwise; after stripping (f); second cycle plating (g−i) where new Li grains are denoted by yellow arrows in (h); and after final stripping (j) where stripped grains are outlined. Full image sequence available as Supporting Information file 002 (electron dose per image = 50 e^-/nm^2 for c−f and 25 e^-/nm^2 for g−j).

zero-loss peak was evident. Nevertheless, the bright-field STEM imaging with a 14.5 pA, 300 keV beam still exhibited good contrast of the relatively large Li deposits at a low dose rate of less than 10 e^- nm^{-2} s^{-1}. Mass−thickness contrast dominates for these thick liquid layers, and thus, the low-density Li (0.534 g/cm^3) exhibits a unique contrast reversal and appears lighter than the surrounding higher-density liquid electrolyte (1.2 g/cm^3). The light-colored deposits seen in Figures 2−7 were also confirmed to be Li by EELS spectra (see Supporting Information Figure S1).

Galvanostatically controlled current was applied to a small (0.26 μm^2) titanium working electrode to induce Li deposition. After a set time period, the current polarity was immediately reversed to strip the deposited Li until the voltage monitored *versus* a Ti quasireference electrode became positive, signaling complete stripping of connected Li. Between cycles, a controlled current of 0 pA was applied to allow the system to relax under open-circuit conditions. In a practical commercial Li battery with 1 to 10 C/cm^2 of cyclable Li, current densities (J) range from 0.3 to 3 mA/cm^2 for charging in an hour. In this study, 6 C/cm^2 was deposited each cycle at varying current densities of 1, 10, and 25 mA/cm^2 normalized to the Ti area on separate, structurally identical Ti electrodes. The electrodeposition results presented here were obtained in one sample on different electrodes to ensure direct comparison. Similar experiments on other samples and other electrodes exhibited the same behavior, shown in the Supporting Information.

Two lithium electrodeposition/stripping cycles performed at 10 mA/cm^2 are shown in Figure 2. No STEM imaging was performed during the first half of the deposition cycle. Thereafter, images were taken every minute (0.6 C/cm^2 deposited between images) during the subsequent deposition and stripping. The complete frame sequence of the deposition and stripping cycles is available as a movie (Supporting Information file 002), and selected images showing the major morphological changes are presented in Figure 2 as well as the chronopotentiometry. The voltage was measured relative to a large-area Ti quasireference electrode, and the inferred voltage *versus* Li is also presented based on

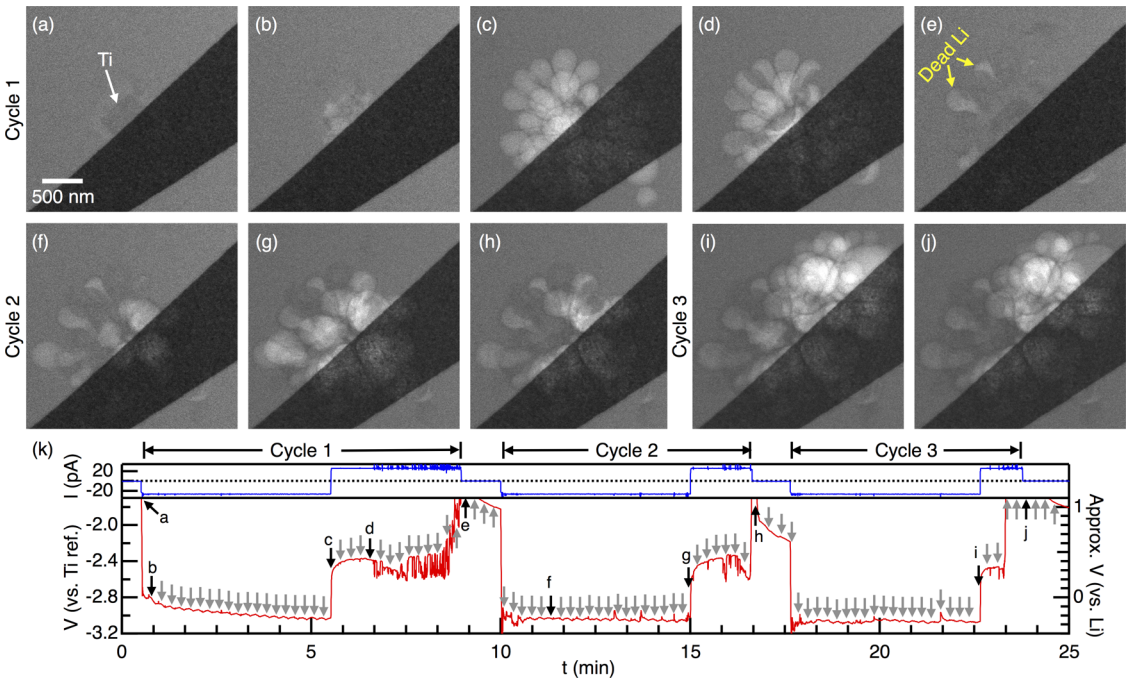

Figure 3. Li cycling at $|J| = 10$ mA/cm^2 while imaging every 15 s. (a) BF STEM image before deposition, (b,c) near the beginning and end of deposition cycle 1, (d,e) near the beginning and end of stripping cycle 1 where disconnected "dead" Li is evident after stripping finished, (f,g) during the second deposition, (h) after the second stripping, (i) after the third deposition, (j) after the third stripping, and (k) chronopotentiometry during cycling with the voltage measured *vs* Ti and inferred *vs* Li; a STEM image was taken at every arrow. Full image sequence available as Supporting Information file 003 (electron dose per image = 50 e^-/nm^2).

the approximate voltage at which Li deposition was observed in the images. However, one should note that this voltage is a very approximate value *versus* Li due to possible drift or polarization of the quasireference electrode during the experiment.

The initial Li deposit (formed without beam exposure in Figure 2c) showed faceted edges and consisted of only one grain. Upon beam exposure, the deposition potential became more negative, dropping by 50–150 mV, and more electrochemical noise occurred. After imaging, the grain bulged and became more circular/spherical in Figure 2d, and upon further growth and imaging in Figure 2e, more grains nucleated including a faintly visible needle emphasized by yellow dotted lines. (The needle is more visible with adjusted image contrast and false coloring, but the images presented here are minimally processed to allow visual estimation of 3D morphology.) The Li needle subsequently rotated clockwise, pointing toward the lower left in Figure 2h–j, likely pushed by new grains deposited at its base. The first stripping cycle only lasted 166 s, implying a low Coulombic efficiency of 27.7%, but it is evident in Figure 2f that a large amount of the Li remained as disconnected "dead" Li. Essentially, the deposit in Figure 2f is the same as in Figure 2d, but it was moved by the extra grains in Figure 2e that did strip away. Cycle 2 showed a much more granular, needle-like morphology seen as the first image in Figure 2g, while subsequent images in Figure 2h,i reveal new spherical grains that grew rather than the needle-like grains formed before imaging. Again, the Coulombic efficiency was low with only a few of the grains stripping in Figure 2j.

On the basis of the results in Figure 2, the electron beam exposure clearly changed the deposition morphology and kinetics to some extent. Without beam exposure, deposited grains show faceting and needle-like morphology, but after exposure to the beam, the growth of any given grain becomes more uniform with a presumably spherical geometry. Furthermore, the beam also causes the nucleation of new grains that may disrupt the growth of the initial grains by electrical disconnection. The movement of Li needles observed here can be understood as new grains depositing near the electrode, pushing the already formed needles away.

To demonstrate the electron beam's influence on Li growth, the plating behavior was recorded during nearly constant beam exposure at a different fresh electrode, again at 10 mA/cm^2. Figure 3 shows selected stills from a movie in which frames were taken every 15 s (Supporting Information file 003). Rather than a few large faceted grains, the Li grew as multiple balloon-like nodules from the working electrode, as seen in Figure 3c. During stripping, only a few grains were actively dissolving at a given time, and the uneven voltage at 7 min occurred after some of the grains had been fully removed, implying that an overpotential was required to initiate stripping in previously inactive SEI-passivated grains. Dead Li was

evident after the first cycle, and the second and third cycles initiated completely new grain growth and more dead Li after cycling.

Comparing Figures 2 and 3, in which Li was deposited at the same current density, the deposition morphology is clearly different for *in situ* imaging with little beam exposure than for *operando* imaging where the electron beam mediated the Li growth in this EC:DMC/$LiPF_6$ liquid electrolyte. Though the electron beam may produce highly reducing solvated electrons, we did not observe any beam-induced Li deposition without electrochemical assistance. Instead, it is possible that the electron beam created a variety of reduced radical species in the electrolyte and SEI that attach to the growing Li surface and equalize (and impede) the growth on all facets, leading to more spherical grains. The electron beam generates a unique SEI that does not produce dendrites but rather facilitates multisite nucleation, and during movie imaging, there is no period in which the natural SEI can form on its own. The increased deposition overpotential upon beam exposure also indicates impeded Li transport. Note that the deposition voltage profile in Figure 3k (constant imaging) is rather smooth compared to Figure 2b (sporadic imaging), indicating more constant overpotentials for nucleation and growth under the electron beam. The small oscillation in deposition potential upon imaging could reflect either the beam-induced SEI formation or a slight perturbation of the Ti quasi-reference electrode potential.

To explore the direct effect of the electron beam on the electrolyte, experiments were performed in which only the electrolyte was exposed to the scanned electron beam. For beam exposure solely in the electrolyte and away from any structures, no obvious changes were visible (see Supporting Information Figure S2). This observation is similar to previous results on $LiPF_6$ in EC:DMC.[28] However, when the beam was scanned near a growing Li deposit, beam-induced SEI growth was observed and is shown in Figure 4 and Supporting Information file 004. In this experiment, Li was actively plating at <1 mA/cm^2, and the beam was rastered in a small square in the electrolyte for 15 s between each image at a higher dose rate of 3750 e^- nm^{-2} s^{-1}. On the side of the Li grain closer to the beam exposure, a dark deposit formed and grew. After 5 min of this increased beam exposure, the Li was electrochemically stripped, and the dark deposit remained and even continued to grow after stripping away the Li. Thus, we believe that the Li functioned as a highly reducing substrate for this beam-induced SEI growth. A similar dark deposit was also seen in Figure 2e–h for Li deposited under high levels of beam exposure. The composition of this beam-induced SEI is unknown, and low-loss EELS spectra in the SEI region appeared nearly identical to the electrolyte region. However, we did observe that the SEI was sensitive

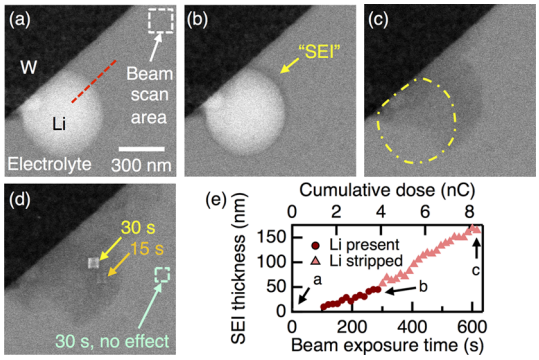

Figure 4. Beam-induced SEI growth. (a) BF STEM image of a Li grain during deposition and nearby 150 nm box for beam scanning in the electrolyte; (b) image after 5 min beam exposure; (c) image after 12 min beam exposure, where the location of the electrochemically stripped Li grain is indicated by a dotted yellow line; (d) image after scanning the beam in 75 nm boxes inside and outside the beam-induced SEI; (e) approximate thickness of the SEI measured along the red dotted line in (a). Full image sequence available as Supporting Information file 004 (electron dose per image = 188 e^-/nm^2; dose rate in beam scan area = 3750 e^- nm^{-2} s^{-1}; dose rate for small squares in (d) = 15 000 e^- nm^{-2} s^{-1}).

to the electron beam. As shown in Figure 4d, the beam was scanned for varying time durations inside three separate small square regions, and the BF STEM contrast in the SEI became lighter than the electrolyte. Thus, we presume that the beam-induced SEI may have consisted of components such as LiF that could be reduced back to metallic Li.[27,36]

Based on these observations, we conclude that the electron beam induces reactive species in the electrolyte that can diffuse to a surface and deposit as a denser, darker material than the electrolyte. Due to the highly reducing Li-metal environment, these species could be the same as those that form a natural SEI such as polymerized carbon chains but at an accelerated rate assisted by the electron beam.[28] A given 300 keV electron passing through the electrolyte may lose tens to hundreds of electronvolts with an average loss *per collision* of about 20 eV (see the Supporting Information), which is large enough to induce reactions not normally accessible. For highly reactive Li deposition, the presence of any SEI (beam-induced or natural) therefore plays a large role in the particle growth by affecting the local flux of Li ions and possibly affecting interfacial energies. In this study, the ~10 pA electron beam current was comparable to the ~10 pA electrochemical currents, so even though most of the electron beam was transmitted, it is not surprising that the electron beam may have significantly affected the electrochemistry. Any beam-induced irreversible reaction products appeared to remain dissolved in solution when far from a Li substrate (Figure S2). However, the observed absence of beam-induced changes in the electrolyte away from any structures was not an unequivocal test to prove that the dose was below a threshold damage limit since the beam clearly

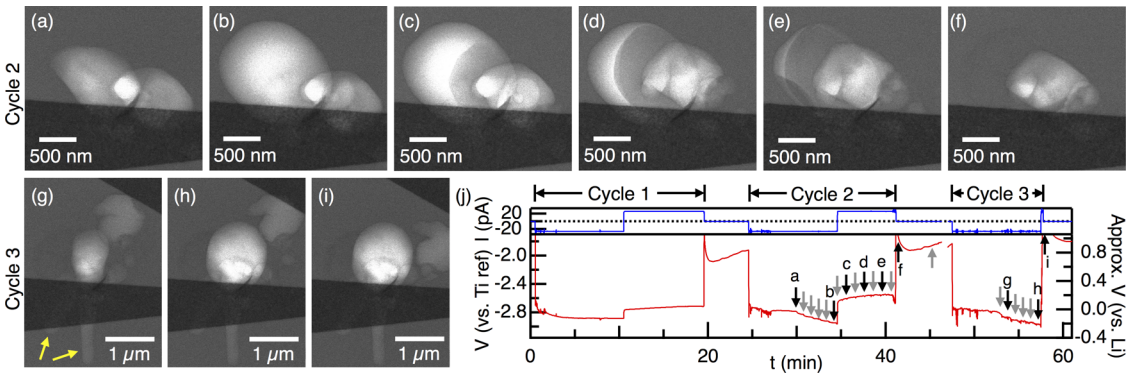

Figure 5. Li cycling at $|J|$ = 10 mA/cm^2, where no imaging was performed during the first deposition/stripping cycle. (a,b) BF STEM images during the second deposition, (c−f) during the second stripping, and (g−i) during the third deposition and stripping where Li needles are indicated with yellow arrows. (j) Chronopotentiometry with voltage measured *vs* Ti and inferred *vs* Li, where arrows indicate the time of each image taken. Full image sequence available as Supporting Information file 005 (electron dose per image = 50 e^-/nm^2 for b,c and 25 e^-/nm^2 for h,i).

affected the Li deposition morphology. Previous accounts of Li electrodeposition in TEM liquid cells have shown "Li" with darker contrast than the surrounding electrolyte,[32,33] and those reported Li deposits were likely covered with a significant beam-induced SEI.

Attempts to image the natural SEI were confounded by the immediate formation of the beam-induced surface film. Even after depositing fresh Li and allowing the sample to equilibrate under open-circuit conditions for a few hours without electron beam exposure, no surface film thicker than 10 nm was evident on the Li. The standard model of a 5−10 nm compact inorganic SEI[37] near the inner Li surface is consistent with our observed 10 nm thickness upper bound. No extended porous organic outer SEI extending ~100 nm[38,39] was observed, though any film possessing a similar density to the electrolyte would exhibit very low contrast. In particular, the dendritic SEI reported in a similar *in situ* liquid TEM cell[33] was not observed.

To further investigate the effects of the electron beam on Li deposition morphology, a third previously unused electrode was cycled with no imaging during the first plating/stripping cycle, still at 10 mA/cm^2. The chronopotentiometry as well as Li morphology during the second and third cycles is shown in Figure 5. Although the morphology was unknown after the first cycle, we observed that the voltage profile during the first plating/stripping cycle was very smooth. For this first cycle, the Coulombic efficiency was 90.2%, indicating that the majority of the deposited Li was stripped. At the beginning of the second deposition cycle, noise in the voltage shows that the SEI mediates Li nucleation even without beam-induced SEI formation. During cycles 2 and 3, imaging was performed periodically as before, and the first image halfway through each deposition cycle again showed faceted grains including needles in cycle 3, whereas after imaging, the grains became more rounded.

The striking Li stripping behavior is especially visible in Figure 5c−f, in which primarily the large rounded grain stripped, and the images again revealed the influence of the SEI for Li electrodes. The dissolution initiated from an isolated point on the right side of the large grain's surface and gradually consumed the grain until another dissolution point was initiated in Figure 5e. Because the SEI forms a protective film around the Li grain, the Li dissolution proceeds only at weak points in the SEI as previously observed by *in situ* AFM.[40] In contrast, materials such as Cu, Ni, or Pb that deposit without passivating surface films have been observed by liquid-cell TEM to subsequently strip much more uniformly where grains simply shrink at every surface.[29,34,41] The uneven Li dissolution behavior contributes to electrode degradation, for dead Li is likely to form if the particle necks off before fully stripping (Figure 3e). In full battery cells, it is known that applied pressure can sometimes electrically reconnect this dead Li.[42]

The cycling and morphology at both lower and higher current densities are shown in Figures 6 (1 mA/cm^2; see also Supporting Information file 006) and 7 (25 mA/cm^2; see also Supporting Information file 007), employing different previously unused electrodes. The total beam exposure and number of images were kept consistent for the various current densities. At 1 mA/cm^2, the deposit is very smooth as expected, with very little overpotential required during deposition and stripping. The Coulombic efficiency was also very high at 84.7 and 91.0% for cycles 1 and 2, respectively, and only 5−20 mV drops in potential were observed upon imaging. Therefore, at the lower current density, the beam effects were less pronounced either because the beam-induced SEI did not limit the lower-rate Li transport or because the longer duration between images allowed time for the surface films to equilibrate. No Li dendrites were observed at 1 mA/cm^2. In contrast, at the higher 25 mA/cm^2 current density, Li needles were observed even on the first cycle prior to imaging, and the Li needles were very pronounced on cycles 2 and 3. After imaging

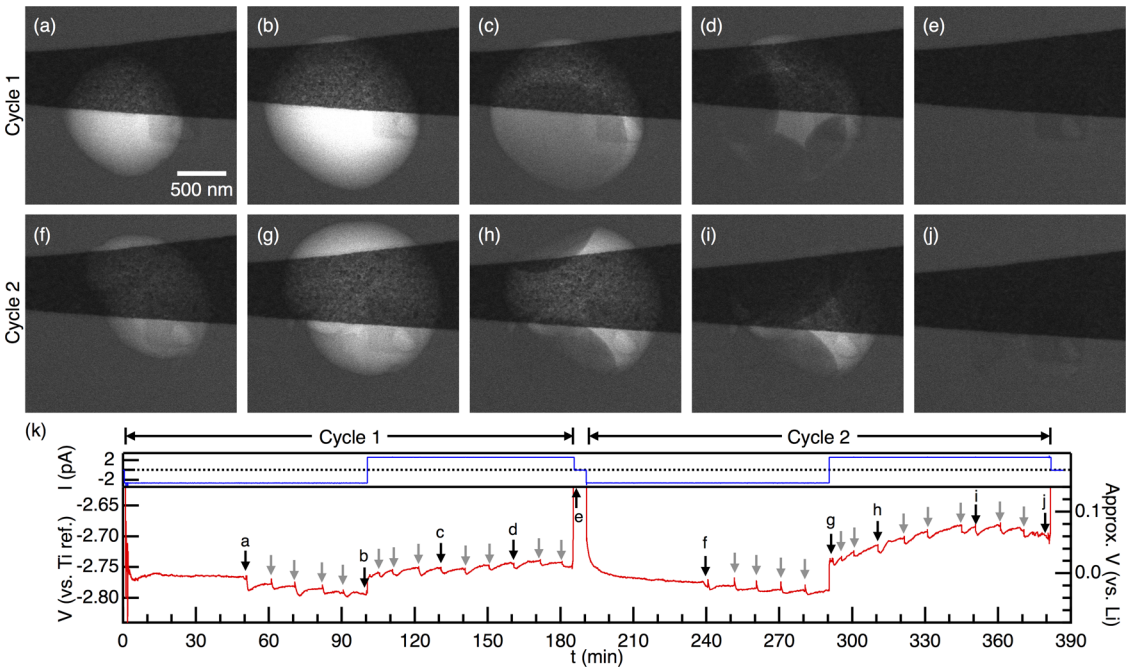

Figure 6. Li cycling at $|J| = 1$ mA/cm^2. (a,b) BF STEM images at midpoint and end point of the first deposition, (c−e) during the first stripping, (f,g) at midpoint and end point of the second deposition, (h−j) during the second stripping, and (k) chronopotentiometry with voltage measured *vs* Ti and inferred *vs* Li, where the time of each image taken is indicated by an arrow. Full image sequence available as Supporting Information file 006 (electron dose per image = 50 e^-/nm^2).

again (Figure 7b,e,h), no new needles were formed, but instead either existing grains grew or new rounded grains nucleated. The Coulombic efficiency at 25 mA/cm^2 was highly varied at 85.5, 8.5, and 73.7% for cycles 1, 2, and 3, respectively, indicating a less-controlled deposition and stripping behavior at this higher current density.

The uniform deposit at low current density allows a visual estimate of the Li deposition efficiency. Assuming the grain in Figure 6b to be a prolate spheroid, its approximate volume of 2.1 μm^3 equates to an ionic charge of 15.6 nC, based on a Li density of 0.534 g/cm^3 and a molecular weight of 6.941 g/mol. Alternatively, the current was controlled at 2.6 pA for 100 min, passing 15.6 nC of electronic charge—encouragingly, exactly equal to the visual estimate. While the geometry is uncertain, this direct correspondence indicates that (i) the electrolyte was very pure with minimal current going to parasitic water, oxygen, or other contaminant reduction; (ii) the unimaged portion of the tungsten electrode was well-masked with all of the electrochemistry occurring in the field of view; (iii) no electrochemical shuttle carrier current existed between the working and nearby Ti counter electrode; (iv) minimal charge was used to form the natural SEI; and (v) the sample wiring was well-isolated with no current passing through parasitic parallel resistances in the chip's fixturing.

On the basis of the results presented here, Li dendrite initiation and growth models can be assessed. As the features observed in this work were very small compared to typical separator-piercing dendrites on the order of 10 μm diameter, these electrochemical TEM observations are relevant to dendrite initiation processes. Although we only imaged a few cycles, whereas practical batteries must survive thousands of cycles, we nevertheless observed that (i) Li needles were formed more readily at a higher current density and not at all at 1 mA/cm^2, and (ii) Li needles were more likely to form on later cycles than on the first cycle. Many dendrite growth models follow Bockris in which diffusion-limited ion transport primarily causes dendrite growth.[43−45] The diffusion-limited current to the small 0.26 μm^2 electrodes in this confined liquid cell is about 10% of the limiting current at a standard ultra-microelectrode of the same size,[34] and for 1 M Li$^+$, the absolute limiting current in the confined cell is on the order of 10 nA (4000 mA/cm^2). Since the largest current used here (65 pA) is orders of magnitude below diffusion limits and Li needles and dendrites were still initiated, we conclude that the diffusion-limited models are more applicable to dendrite propagation than initiation.[9] We further note that no preferred direction for Li needles was observed, and the location of the counter electrode did not determine the growth direction. Alternative models consider the limiting current to be determined by slower Li$^+$ diffusion through the SEI such that defects in the SEI provide a higher Li$^+$ flux and initiate dendrites.[8] In light of our results, we believe the SEI's composition,[46] heterogeneity,[47] role in modifying interfacial energies,[48] and Li$^+$ surface transport properties[49] are critical components to include in dendrite initiation models. The propensity for

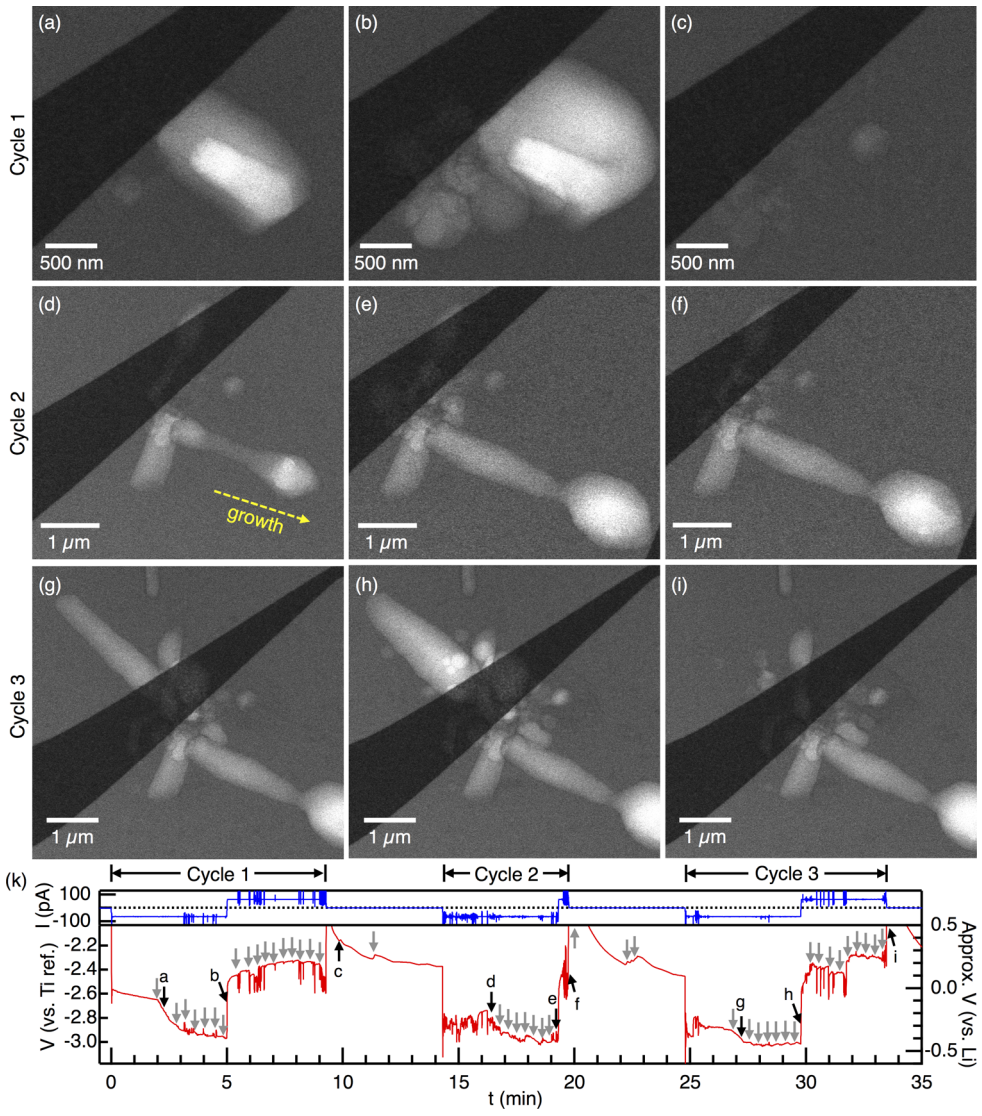

Figure 7. Li cycling at $|J| = 25$ mA/cm^2. Images are shown at midpoint (left) and end point (center) of each deposition cycle as well as after stripping (right); little appreciable stripping occurred on cycle 2. Chronopotentiometry with voltage measured *vs* Ti and inferred *vs* Li shown in (k) where the time of each image taken is indicated by an arrow. A Li needle indicated in (d) grew outward and thickened during deposition. Full image sequence available as Supporting Information file 007 (electron dose per image = 25 e^-/nm^2 for a–c and 12.5 e^-/nm^2 for d–i).

needles to form on the second or third cycle can be understood by the development of a thicker heterogeneous natural and/or beam-induced SEI after the first cycle. The lack of needles at 1 mA/cm^2 may imply a boundary on the limiting diffusion flux through the SEI or an SEI equilibration time, though more work is required to separate the effects of the beam-induced SEI from the natural SEI formed in the absence of imaging. A contrasting model for Li whisker growth was developed by Yamaki,[50] in which soft Li is extruded through a defect in the SEI, resulting in growth from the base rather than the tip. In this work, we observed at least one Li needle appear to grow from the base, shown in Figure 7d,e, but that growth could also be explained by Li insertion at a crystal defect somewhere along the needle.[6]

The conditions in the TEM liquid cell likely enhanced dendrite formation compared to a macroscale battery, due to the large electrolyte volume to electrode area ratio, radial diffusion, lack of separator pressure, and beam-induced SEI effects. Nevertheless, the trends observed here should hold for actual batteries, perhaps with dendrites appearing at later cycles and lower values of current density.

In this study, we employed a Ti quasireference electrode. However, in principle, a more quantitative analysis of the voltage fluctuations observed during deposition and imaging is possible with a better-defined reference electrode. We explored the possibility of depositing *in situ* a Li reference electrode by galvanostatic Li deposition and subsequently changing the electrode connections. Indeed, the table of contents/abstract figure shows the results obtained with this type of Li reference electrode. However, in practice, we discovered that the relatively small Li

reference electrode lifetime was limited to approximately an hour before its potential started to drift.

We chose to use EC:DMC/$LiPF_6$ as a common liquid battery electrolyte, but other compositions are likely more optimal for Li electrodeposition. Future studies include Li deposition and SEI dynamics in alternative electrolytes such as dioxolane, which is known to form more uniform Li deposits[51] or additives such as vinylene carbonate that promote a stable SEI.[52] Addition of "artificial SEI" surface films on the electrodes is also possible, which has been shown to increase Li cycling efficiency.[53]

CONCLUSIONS

The Li electrodeposition dynamics in liquid EC:DMC/$LiPF_6$ electrolyte were imaged *via* STEM with unprecedented clarity, and the electron beam was found to affect the morphology even at low dose. At a constant current density of 10 mA/cm^2, the Li deposits formed faceted crystals and needles without beam exposure or rounded nodules with beam exposure. At a lower current density of 1 mA/cm^2, the electron beam exposure had less of an effect on morphology and cycling efficiency, and larger grains were formed. At a higher current density of 25 mA/cm^2, many small needle-like crystals were formed after the first cycle. Electron irradiation produces solid SEI deposits that alter growth dynamics, a process consistent with beam-induced radical formation in the electrolyte followed by transport to and reaction at the growing Li interface. During electrochemical stripping, the dissolution clearly initiated from discrete points on the Li grains, leaving behind beam-induced SEI and, in some instances, dead Li that was spatially and electrically isolated from the current collector. Our results show that the SEI plays a critical role in Li dendrite initiation. For *in situ* liquid-cell TEM studies, we conclude that *operando* imaging of active electrochemical processes should be performed with caution due to beam effects, but *in situ* imaging after performing the electrochemistry can still provide unique nanoscale insights into electrodeposition processes and morphology.

METHODS

The TEM liquid-cell construction and assembly are described in detail elsewhere.[34] Briefly, silicon chips were coated with 30 nm SiN_x, and 30 μm diameter view holes were etched *via* a Bosch process up to the suspended membrane. On the bottom chips, ten 1500 μm^2 electrodes consisting of 50 nm thick W on 25 nm thick TiN converged to the center of the membrane, as seen in Figure 1c,d, and doped poly-Si leads were buried beneath the SiN_x layer and encased in insulating SiO_2 that connected the metal electrodes to the external bond pads. The metal electrodes were passivated by 33 nm thick ALD-deposited Al_2O_3 and 7 nm thick sputter-deposited SiO_2, similar to a previous design with partially exposed electrodes.[54] The smaller Ti thin-film electrodes visible in Figure 1c–e were patterned by a sequence of electron beam lithography in poly(methyl methacrylate), wet etching in 2.3% hydrofluoric acid/11.4% ammonium fluoride/19.6% water/66.7% ethylene glycol by volume to remove the passivation layer, and electron beam evaporation of 35 nm Ti followed by liftoff. A raised 1.6 × 0.7 mm^2 poly-Si seal ring on the bottom chip defined the separation between the bottom chip and the lid as well as defined a boundary between the liquid reservoir and the epoxy seal. The lid chip had a similar suspended SiN_x membrane in the center as well as two holes etched for fluid filling. The top and bottom chips were aligned by placing appropriately sized alignment beads in pyramidal KOH etch pits in the Si such that the view windows overlapped. A line of epoxy (Loctite Hysol 1C-LV) placed between the two chips (white line in Figure 1a) wicked up to the seal ring upon curing at 70 °C.

After assembly, the chip was wire-bonded to a ceramic chip carrier that fit into a multiple-lead TEM holder (Nanofactory Instruments AB). The liquid filling was performed in a He-filled glovebox with O_2 and H_2O levels maintained below 10 ppm. The electrolyte consisted of 1:1 by volume ethylene carbonate/dimethyl carbonate with 1 M $LiPF_6$ obtained from Novolyte Technologies, Inc. A droplet of electrolyte was placed at one fill port such that it wicked into the chamber, the excess wiped away, and small pieces of polyimide tape were placed over both fill ports. Subsequently, quick-cure epoxy (Scotch DP-100) was spread over the tape-covered fill ports and allowed to cure at least an hour in the glovebox before loading in the TEM.

A Modulab potentiostat (Ametek, Inc.) fitted with a femtoammeter was used in galvanostatic mode to apply current and measure potentials. The cabling was fully shielded and the working electrode guarded up to the TEM column, and the potentiostat was internally grounded (all cell components were isolated from ground in our cell/holder design). A custom-designed, battery-powered voltage buffer preamplifier was used on the reference electrode to lower its current draw to less than 10 fA. The active area of the Ti working electrode measured by scanning electron microscopy was 0.26 μm^2, so absolute currents of 2.6, 26, and 65 pA were used to achieve current densities of 1, 10, and 25 mA/cm^2, respectively. "Open-circuit" voltage was measured in galvanostatic mode with 0 pA applied to avoid polarizing the small working electrodes with current draw from the reference electrode. The counter electrode voltage was also monitored *versus* the Li-depositing working electrode and typically approached 4 to 6 V, indicating that oxidative electrolyte decomposition at the counter electrode supported the applied current.

Imaging was performed on a FEI Tecnai F30 TEM/STEM operated at 300 kV in BF STEM mode. The beam current was 14.5 pA with a 8.4 mrad convergence angle. The beam was blanked between images. Each image was acquired with 1024 × 1024 pixels over 5 s with a field of view of 3 × 3 μm^2 or larger, so the typical dose rate was 10 e^- nm^{-2} s^{-1} = 0.1 e^- Å^{-2} s^{-1} and a total dose of 50 e^- nm^{-2} fr^{-1} = 72 pC/fr or less. For the beam-induced SEI growth experiment shown in Figure 4, slightly different conditions were used on a separate sample: a 13.5 pA beam with a 1.5 × 1.5 μm^2 field for imaging every 30 s at 37.5 e^- nm^{-2} s^{-1} and a smaller "focus" square of 150 × 150 nm^2 exposed for 15 s between images at 100× higher dose rate; at each image, 203 pC of electron beam passed through the "focus" square. Beam exposure apart from imaging was minimized; an initial image was taken of each electrode, then the beam was blanked for at least 5 min before initiating the electrochemistry. About 350 total images over 12 h were taken during the experiments shown in Figures 2, 3, 5, and 6.

Conflict of Interest: The authors declare no competing financial interest.

Acknowledgment. We would like to thank Sean Hearne and Gary Rubloff for project support, Michael Shaw and the Sandia MESA CMOS fabrication facility for design and production of the TEM liquid cells, and Nick Hudak, Kyle Fenton, and Kevin Leung for advice on Li-ion electrochemistry and procedures. This work was performed at the Center for Integrated Nanotechnologies

(CINT), an Office of Science User Facility operated for the U.S. Department of Energy (DOE) Office of Science. Sandia National Laboratories is a multiprogram laboratory managed and operated by Sandia Corporation, a wholly owned subsidiary of Lockheed Martin Corporation, for the U.S. Department of Energy's National Nuclear Security Administration under Contract DE-AC04-94AL85000. This work was supported in part by a Laboratory Directed Research and Development (LDRD) project at Sandia National Laboratories (SNL) and in part by Nanostructures for Electrical Energy Storage (NEES), an Energy Frontier Research Center (EFRC) funded by the U.S. Department of Energy, Office of Science, Office of Basic Energy Sciences under Award Number DESC0001160. The LDRD supported the development and fabrication of platforms. The NEES center supported the development of TEM techniques.

Supporting Information Available: EELS spectra of the Li and electrolyte, beam-induced effects solely on the electrolyte away from Li, Li plating images from other samples showing reproducibility, and calculations of average energy loss of the 300 kV electron beam in the liquid layer. Videos containing the full image sequences of Li electrodeposition and stripping. This material is available free of charge *via* the Internet at http://pubs.acs.org.

Note Added after ASAP Publication: This paper was published ASAP March 24, 2015. The fifth author was designated as a corresponding author after Editorial review and approval. The revised version was reposted March 26, 2015.

REFERENCES AND NOTES

1. *Linden's Handbook of Batteries*, 4th ed.; Reddy, T. B., Linden, D., Eds.; McGraw-Hill: New York, 2011.
2. Kim, H.; Jeong, G.; Kim, Y.-U.; Kim, J.-H.; Park, C.-M.; Sohn, H.-J. Metallic Anodes for Next Generation Secondary Batteries. *Chem. Soc. Rev.* **2013**, *42*, 9011.
3. Aurbach, D. A Short Review of Failure Mechanisms of Lithium Metal and Lithiated Graphite Anodes in Liquid Electrolyte Solutions. *Solid State Ionics* **2002**, *148*, 405–416.
4. Li, Z.; Huang, J.; Yann Liaw, B.; Metzler, V.; Zhang, J. A Review of Lithium Deposition in Lithium-Ion and Lithium Metal Secondary Batteries. *J. Power Sources* **2014**, *254*, 168–182.
5. Peled, E.; Golodnitsky, D.; Ardel, G. Advanced Model for Solid Electrolyte Interphase Electrodes in Liquid and Polymer Electrolytes. *J. Electrochem. Soc.* **1997**, *144*, L208–L210.
6. Steiger, J.; Kramer, D.; Mönig, R. Mechanisms of Dendritic Growth Investigated by *In Situ* Light Microscopy during Electrodeposition and Dissolution of Lithium. *J. Power Sources* **2014**, *261*, 112–119.
7. Stark, J. K.; Ding, Y.; Kohl, P. A. Nucleation of Electrodeposited Lithium Metal: Dendritic Growth and the Effect of Co-deposited Sodium. *J. Electrochem. Soc.* **2013**, *160*, D337–D342.
8. Nishikawa, K.; Mori, T.; Nishida, T.; Fukunaka, Y.; Rosso, M.; Homma, T. *In Situ* Observation of Dendrite Growth of Electrodeposited Li Metal. *J. Electrochem. Soc.* **2010**, *157*, A1212.
9. Crowther, O.; West, A. C. Effect of Electrolyte Composition on Lithium Dendrite Growth. *J. Electrochem. Soc.* **2008**, *155*, A806.
10. Harry, K. J.; Hallinan, D. T.; Parkinson, D. Y.; MacDowell, A. A.; Balsara, N. P. Detection of Subsurface Structures underneath Dendrites Formed on Cycled Lithium Metal Electrodes. *Nat. Mater.* **2013**, *13*, 69–73.
11. Dollé, M.; Sannier, L.; Beaudoin, B.; Trentin, M.; Tarascon, J.-M. Live Scanning Electron Microscope Observations of Dendritic Growth in Lithium/Polymer Cells. *Electrochem. Solid-State Lett.* **2002**, *5*, A286.
12. Orsini, F.; du Pasquier, A.; Beaudouin, B.; Tarascon, J. M.; Trentin, M.; Langenhuizen, N.; de Beer, E.; Notten, P. *In Situ* SEM Study of the Interfaces in Plastic Lithium Cells. *Electrochim. Acta* **1999**, *81*−*82*, 918–921.
13. Chen, D.; Indris, S.; Schulz, M.; Gamer, B.; Mönig, R. *In Situ* Scanning Electron Microscopy on Lithium-Ion Battery Electrodes Using an Ionic Liquid. *J. Power Sources* **2011**, *196*, 6382–6387.
14. Shao, M. *In Situ* Microscopic Studies on the Structural and Chemical Behaviors of Lithium-Ion Battery Materials. *J. Power Sources* **2014**, *270*, 475–486.
15. Liu, X. H.; Liu, Y.; Kushima, A.; Zhang, S.; Zhu, T.; Li, J.; Huang, J. Y. *In Situ* TEM Experiments of Electrochemical Lithiation and Delithiation of Individual Nanostructures. *Adv. Energy Mater.* **2012**, *2*, 722–741.
16. Noh, K. W.; Dillon, S. J. Morphological Changes in and around Sn Electrodes during Li Ion Cycling Characterized by *In Situ* Environmental TEM. *Scripta Mater.* **2013**, *69*, 658–661.
17. Gu, M.; Parent, L. R.; Mehdi, B. L.; Unocic, R. R.; McDowell, M. T.; Sacci, R. L.; Xu, W.; Connell, J. G.; Xu, P.; Abellan, P.; et al. Demonstration of an Electrochemical Liquid Cell for Operando Transmission Electron Microscopy Observation of the Lithiation/Delithiation Behavior of Si Nanowire Battery Anodes. *Nano Lett.* **2013**, *13*, 6106–6112.
18. Holtz, M. E.; Yu, Y.; Gunceler, D.; Gao, J.; Sundararaman, R.; Schwarz, K. A.; Arias, T. A.; Abruña, H. D.; Muller, D. A. Nanoscale Imaging of Lithium Ion Distribution during *In Situ* Operation of Battery Electrode and Electrolyte. *Nano Lett.* **2014**, *14*, 1453–1459.
19. Zheng, H.; Smith, R. K.; Jun, Y. W.; Kisielowski, C.; Dahmen, U.; Alivisatos, A. P. Observation of Single Colloidal Platinum Nanocrystal Growth Trajectories. *Science* **2009**, *324*, 1309–1312.
20. Evans, J. E.; Jungjohann, K. L.; Browning, N. D.; Arslan, I. Controlled Growth of Nanoparticles from Solution with *In Situ* Liquid Transmission Electron Microscopy. *Nano Lett.* **2011**, *11*, 2809–2813.
21. Noh, K. W.; Liu, Y.; Sun, L.; Dillon, S. J. Challenges Associated with *In-Situ* TEM in Environmental Systems the Case of Silver in Aqueous Solutions. *Ultramicroscopy* **2012**, *116*, 34–38.
22. Liao, H. G.; Zherebetskyy, D.; Xin, H.; Czarnik, C.; Ercius, P.; Elmlund, H.; Pan, M.; Wang, L. W.; Zheng, H. Facet Development during Platinum Nanocube Growth. *Science* **2014**, *345*, 916–919.
23. Li, D.; Nielsen, M. H.; Lee, J. R. I.; Frandsen, C.; Banfield, J. F.; De Yoreo, J. J. Direction-Specific Interactions Control Crystal Growth by Oriented Attachment. *Science* **2012**, *336*, 1014–1018.
24. Jungjohann, K. L.; Bliznakov, S.; Sutter, P. W.; Stach, E. A.; Sutter, E. A. *In Situ* Liquid Cell Electron Microscopy of the Solution Growth of Au−Pd Core−Shell Nanostructures. *Nano Lett.* **2013**, *13*, 2964–2970.
25. Grogan, J. M.; Schneider, N. M.; Ross, F. M.; Bau, H. H. Bubble and Pattern Formation in Liquid Induced by an Electron Beam. *Nano Lett.* **2014**, *14*, 359–364.
26. Lewis, E. A.; Haigh, S. J.; Slater, T. J. A.; He, Z.; Kulzick, M. A.; Burke, M. G.; Zaluzec, N. J. Real-Time Imaging and Local Elemental Analysis of Nanostructures in Liquids. *Chem. Commun.* **2014**, *50*, 10019–10022.
27. Yuk, J. M.; Seo, H. K.; Choi, J. W.; Lee, J. Y. Anisotropic Lithiation Onset in Silicon Nanoparticle Anode Revealed by *In Situ* Graphene Liquid Cell Electron Microscopy. *ACS Nano* **2014**, *8*, 7478–7485.
28. Abellan, P.; Mehdi, B. L.; Parent, L. R.; Gu, M.; Park, C.; Xu, W.; Zhang, Y.; Arslan, I.; Zhang, J.-G.; Wang, C.-M.; et al. Probing the Degradation Mechanisms in Electrolyte Solutions for Li-Ion Batteries by *In Situ* Transmission Electron Microscopy. *Nano Lett.* **2014**, *14*, 1293–1299.
29. White, E. R.; Singer, S. B.; Augustyn, V.; Hubbard, W. A.; Mecklenburg, M.; Dunn, B.; Regan, B. C. *In Situ* Transmission Electron Microscopy of Lead Dendrites and Lead Ions in Aqueous Solution. *ACS Nano* **2012**, *6*, 6308–6317.
30. Williamson, M. J.; Tromp, R. M.; Vereecken, P. M.; Hull, R.; Ross, F. M. Dynamic Microscopy of Nanoscale Cluster Growth at the Solid−Liquid Interface. *Nat. Commun.* **2003**, *2*, 532–536.

31. Radisic, A.; Ross, F. M.; Searson, P. C. *In Situ* Study of the Growth Kinetics of Individual Island Electrodeposition of Copper. *J. Phys. Chem. B* **2006**, *110*, 7862–7868.
32. Zeng, Z.; Liang, W.-I.; Liao, H.-G.; Xin, H. L.; Chu, Y.-H.; Zheng, H. Visualization of Electrode–Electrolyte Interfaces in $LiPF_6$/EC/DEC Electrolyte for Lithium Ion Batteries *via In Situ* TEM. *Nano Lett.* **2014**, *14*, 1745–1750.
33. Sacci, R. L.; Dudney, N. J.; More, K. L.; Parent, L. R.; Arslan, I.; Browning, N. D.; Unocic, R. R. Direct Visualization of Initial SEI Morphology and Growth Kinetics during Lithium Deposition by *In Situ* Electrochemical Transmission Electron Microscopy. *Chem. Commun.* **2014**, *50*, 2104–2107.
34. Leenheer, A. J.; Sullivan, J. P.; Shaw, M. J.; Harris, C. T. A Sealed Liquid Cell for *In Situ* Transmission Electron Microscopy of Controlled Electrochemical Processes. *J. Microelectromech. Syst.* **2015**, 10.1109/JMEMS.2014.2380771.
35. Schneider, N. M.; Norton, M. M.; Mendel, B. J.; Grogan, J. M.; Ross, F. M.; Bau, H. H. Electron–Water Interactions and Implications for Liquid Cell Electron Microscopy. *J. Phys. Chem. C* **2014**, *118*, 22373–22382.
36. Ghatak, J.; Guan, W.; Möbus, G. *In Situ* TEM Observation of Lithium Nanoparticle Growth and Morphological Cycling. *Nanoscale* **2012**, *4*, 1754.
37. Lu, P.; Li, C.; Schneider, E. W.; Harris, S. J. Chemistry, Impedance, and Morphology Evolution in Solid Electrolyte Interphase Films during Formation in Lithium Ion Batteries. *J. Phys. Chem. C* **2014**, *118*, 896–903.
38. Andersson, A. M.; Henningson, A.; Siegbahn, H.; Jansson, U.; Edström, K. Electrochemically Lithiated Graphite Characterised by Photoelectron Spectroscopy. *J. Power Sources* **2003**, *119–121*, 522–527.
39. Hirasawa, K. A. *In Situ* Electrochemical Atomic Force Microscope Study on Graphite Electrodes. *J. Electrochem. Soc.* **1997**, *144*, L81.
40. Aurbach, D.; Cohen, Y. *In Situ* Micromorphological Studies of Li Electrodes by Atomic Force Microscopy in a Glove Box System. *Electrochem. Solid-State Lett.* **1999**, *2*, 16–18.
41. Chen, X.; Noh, K. W.; Wen, J. G.; Dillon, S. J. *In Situ* Electrochemical Wet Cell Transmission Electron Microscopy Characterization of Solid–Liquid Interactions between Ni and Aqueous $NiCl_2$. *Acta Mater.* **2012**, *60*, 192–198.
42. Gireaud, L.; Grugeon, S.; Laruelle, S.; Yrieix, B.; Tarascon, J. M. Lithium Metal Stripping/Plating Mechanisms Studies: A Metallurgical Approach. *Electrochem. Commun.* **2006**, *8*, 1639–1649.
43. Diggle, J. W.; Despic, A. R.; Bockris, J. O. The Mechanism of the Dendritic Electrocrystallization of Zinc. *J. Electrochem. Soc.* **1969**, *116*, 1503.
44. Monroe, C.; Newman, J. Dendrite Growth in Lithium/Polymer Systems. *J. Electrochem. Soc.* **2003**, *150*, A1377.
45. Tikekar, M. D.; Archer, L. A.; Koch, D. L. Stability Analysis of Electrodeposition Across a Structured Electrolyte with Immobilized Anions. *J. Electrochem. Soc.* **2014**, *161*, A847–A855.
46. López, C. M.; Vaughey, J. T.; Dees, D. W. Insights Into the Role of Interphasial Morphology on the Electrochemical Performance of Lithium Electrodes. *J. Electrochem. Soc.* **2012**, *159*, A873.
47. Rosso, M.; Gobron, T.; Brissot, C.; Chazalviel, J. N.; Lascaud, S. Onset of Dendritic Growth in Lithium/Polymer Cells. *J. Power Sources* **2001**, *97–98*, 804–806.
48. Ely, D. R.; Garcia, R. E. Heterogeneous Nucleation and Growth of Lithium Electrodeposits on Negative Electrodes. *J. Electrochem. Soc.* **2013**, *160*, A662–A668.
49. Steiger, J.; Richter, G.; Wenk, M.; Kramer, D.; Mönig, R. Comparison of the Growth of Lithium Filaments and Dendrites under Different Conditions. *Electrochem. Commun.* **2015**, *50*, 11.
50. Yamaki, J.-I.; Tobishima, S.-I.; Hayashi, K.; Saito, K.; Nemoto, Y.; Arakawa, M. A Consideration of the Morphology of Electrochemically Deposited Lithium in an Organic Electrolyte. *J. Power Sources* **1998**, *74*, 219–227.
51. Aurbach, D.; Zinigrad, E.; Teller, H.; Cohen, Y.; Salitra, G.; Yamin, H.; Dan, P.; Elster, E. Attempts To Improve the Behavior of Li Electrodes in Rechargeable Lithium Batteries. *J. Electrochem. Soc.* **2002**, *149*, A1267–A1277.
52. Xu, K. Nonaqueous Liquid Electrolytes for Lithium-Based Rechargeable Batteries. *Chem. Mater.* **2004**, *104*, 4303–4418.
53. Yan, K.; Lee, H.-W.; Gao, T.; Zheng, G.; Yao, H.; Wang, H.; Lu, Z.; Zhou, Y.; Liang, Z.; Liu, Z.; et al. Ultrathin Two-Dimensional Atomic Crystals as Stable Interfacial Layer for Improvement of Lithium Metal Anode. *Nano Lett.* **2014**, *14*, 6016–6022.
54. Grogan, J. M.; Bau, H. H. The Nanoaquarium: A Platform for *In Situ* Transmission Electron Microscopy in Liquid Media. *J. Microelectromech. Syst.* **2010**, *19*, 885–894.